THE FASEB JOURNAL • RESEARCH • www.fasebj.org

Connexin 43 gap junctions contribute to brain endothelial barrier hyperpermeability in familial cerebral cavernous malformations type III by modulating tight junction structure

Allison M. Johnson,* James P. Roach,† Anna Hu,* Svetlana M. Stamatovic,* Michal R. Zochowski,‡ Richard F. Keep,§,¶ and Anuska V. Andjelkovic*,§,1

*Department of Pathology, §Department of Neurosurgery, †Neuroscience Graduate Program, and ¶Department of Molecular and Integrative Physiology, Medical School, University of Michigan, Ann Arbor, Michigan, USA; and ‡Department of Physics and Biophysics, University of Michigan, Ann Arbor, Michigan, USA

ABSTRACT: Familial cerebral cavernous malformations type III (fCCM3) is a disease of the cerebrovascular system caused by loss-of-function mutations in *ccm3* that result in dilated capillary beds that are susceptible to hemorrhage. Before hemorrhage, fCCM3 lesions are characterized by a hyperpermeable blood-brain barrier (BBB), the key pathologic feature of fCCM3. We demonstrate that connexin 43 (Cx43), a gap junction (GJ) protein that is incorporated into the BBB junction complex, is up-regulated in lesions of a murine model of fCCM3. Small interfering RNA–mediated *ccm3* knockdown (CCM3KD) in brain endothelial cells *in vitro* increased Cx43 protein expression, GJ plaque size, GJ intracellular communication (GJIC), and barrier permeability. CCM3KD hyperpermeability was rescued by GAP27, a peptide gap junction and hemichannel inhibitor of Cx43 GJIC. Tight junction (TJ) protein, zonula occludens 1 (ZO-1), accumulated at Cx43 GJs in CCM3KD cells and displayed fragmented staining at TJs. The GAP27-mediated inhibition of Cx43 GJs in CCM3KD cells restored ZO-1 to TJ structures and reduced plaque accumulation at Cx43 GJs. The TJ protein, Claudin-5, was also fragmented at TJs in CCM3KD cells, and GAP27 treatment lengthened TJ-associated fragments and increased Claudin 5–Claudin 5 transinteraction. Overall, we demonstrate that Cx43 GJs are aberrantly increased in fCCM3 and regulate barrier permeability by a TJ-dependent mechanism.—Johnson, A. M., Roach, J. P., Hu, A., Stamatovic, S. M., Zochowski, M. R., Keep, R. F., Andjelkovic, A. V. Connexin 43 gap junctions contribute to brain endothelial barrier hyperpermeability in familial cerebral cavernous malformations type III by modulating tight junction structure. FASEB J. 32, 2615–2629 (2018). www.fasebj.org

KEY WORDS: permeability · PDCD10 · cell-cell interaction · zonula occludens-1

Familial cerebral cavernous malformations type III (fCCM3) is a disease that affects cerebrovascular capillary beds. Patients carry a null mutation in one allele of *ccm3* (*pdcd*10). Lesions—characterized by dilated vessels, blood-filled caverns, loss of contact between endothelial cells, and insufficient blood-brain barrier (BBB) integrity—are initiated upon acquiring a mutation in the second *ccm3* allele that causes a loss of functional CCM3 protein. Impaired BBB integrity is considered the primary cause of fCCM3 morbidities, including seizures, focal neurologic deficits, and cerebral hemorrhage (1). No effective treatment is available to patients with fCCM3, and therapeutic development is hindered by a lack of a thorough understanding of CCM3-dependent pathways. Proteomic analysis has revealed that 80% of CCM3 is bound to the striatin-interacting phosphatase and kinase (STRIPAK) complex (2). This complex contains many phosphatases and kinases that produce wide-ranging cellular effects, including Golgi apparatus development, calcium sensing, and, most recently, a CCM3-dependent effect on actin cytoskeleton organization that is mediated by cortactin (3, 4).

BBB integrity is maintained by a unique junction complex at the endothelial–endothelial border that

ABBREVIATIONS: BBB, blood-brain barrier; CCM3KD, small interfering RNA–mediated *ccm3* knockdown; Cx, connexin; Cx43, connexin 43; fCCM3, familial cerebral cavernous malformations type III; FRAP, fluorescence recovery after photobleaching; FRET, fluorescence resonance energy transfer; GAP19, Cx43 hemichannel inhibitor; GAP27, Cx43 gap junction and hemichannel inhibitor; Gd-DTPA, gadolinium-DTPA; GJ, gap junction; GJIC, gap junction intercellular communication; HC, hemichannel; LY, Lucifer yellow; mBEC, microvascular brain endothelial cell; ROI, region of interest; siRNA, small interfering RNA; STRIPAK, striatin-interacting phosphatase and kinase; TE, echo time; TEER, transendothelial electrical resistance; TJ, tight junction; TR, repetition time; ZO-1, zonula occludens 1

[1] Correspondence: Department of Pathology, University of Michigan, Medical School, 7520A MSRB I, 1150 W Medical Center Dr., Ann Arbor, MI 48109-5602, USA. E-mail: anuskaa@med.umich.edu

doi: 10.1096/fj.201700699R

This article includes supplemental data. Please visit *http://www.fasebj.org* to obtain this information.

includes adherens junctions, tight junctions (TJs), and gap junctions (GJs). Under normal physiologic conditions, crosstalk mechanisms allow these complexes to form a stable barrier that prevents paracellular permeability. The TJ complex is composed of the transmembrane proteins, claudins and occludin, that form transinteractions with neighboring cell claudins and occludin and occlude the paracellular space. Claudins and occludin are stabilized by intracellular adaptor proteins, including zonula occludens 1 (ZO-1), that tether them to the actin cytoskeleton. Analysis of TJ proteins in lesions of patients with fCCM3 and *in vitro* work has demonstrated a loss of TJ proteins from the junctional complex of fCCM3 (4, 5). Meanwhile, whether adherens junctions, organized in a similar manner to TJs with transmembrane cadherins and adapter proteins, are affected in fCCM3 is less clear (4, 6).

The final member of the BBB junction complex, the GJ, has not been ascribed a regulatory role for paracellular permeability. GJs are channel structures at adjacent cell borders, are formed by members of the connexin family (Cx), and allow direct passage of ions and small molecules that are <1 kDa between the cytosols of adjacent cells. Channels are formed by the aggregation of homo- or hetero-hexameric Cx proteins (7). Cx family members display tissue-specific expression, with Cx37, Cx40, and Cx43 expressed in brain endothelia (8, 9). Aberrant elevation of Cx43 protein has recently been shown to be detrimental to barrier integrity, but whether this effect is dependent on Cx43 GJs or other functions of Cx43, including hemichannels (HCs) that do not directly oppose another Cx43 channel, has not been thoroughly described (10, 11).

We have identified that $ccm3^{+/-}p53^{-/-}$ mice, a murine model of fCCM3, have elevated Cx43 protein expression in lesions. Analysis of Cx43 in CCM3 knockdown (CCM3KD) brain endothelial cells *in vitro* also revealed increased GJ activity and that reducing Cx43 expression and GJ activity rescued the permeability defect in CCM3KD cells. The focus of the current study is to define the mechanism by which Cx43 GJs regulate permeability and establish whether increased Cx43 protein is a primary defect in the maturation of CCM3 lesions in a mouse model of fCCM3.

MATERIALS AND METHODS

Cell culture

A transformed murine brain microvascular endothelial cell line (mBECs; Angioproteomie, Atlanta, GA, USA) was cultured in growth media (DMEM, 4.5 g/L glucose, 1× L-glutamine, 1× antibiotic-antimycotic, 20% fetal bovine serum) at 37°C and 5% CO_2. All experiments were conducted after 24 h of serum deprivation (DMEM, 4.5 g/L glucose, 1× L-glutamine).

Cell transfection

CCM1, CCM2, CCM3, and Cx43 knockdowns were achieved *via* transfection with Lipofectin (Thermo Fisher Scientific, Waltham, MA, USA); 3 ccm3 small interfering RNAs (siRNAs): silencer select s80540, s80539, s80538 (Thermo Fisher Scientific); Ccm1: siGENOME, D-056854-02-0002; Ccm2: siGENOME, D-057315-02-0002 (Dharmacon, Lafayette, CO, USA); and Cx43: SASI-Mm01-00135298 (PDSIRNA2D; Sigma-Aldrich, St. Louis, MO, USA).

Mouse model of fCCM3

C57BL/6J mice that were heterozygous for *ccm3* ($ccm3^{+/-}$) were obtained from Yale University (New Haven, CT, USA) (6). B6.129S2-$Trp53^{tm1Tyj}$/J mice that carried a null mutation of *p53* ($p53^{-/-}$) were obtained from The Jackson Laboratory (Bar Harbor, ME, USA). $Ccm3^{+/-}$ and $p53^{-/-}$ mice were bred together for two generations to produce $ccm3^{+/-}p53^{-/-}$ mice, which enabled the acquisition of a somatic second hit to *ccm3* (12, 13).

MRI

All mice were anesthetized with 2% isoflurane/air mixture throughout MRI examination. Mice lay prone, head first in a 7.0T or 9.4T Agilent MR scanner (horizontal bore; Agilent Technologies, Palo Alto, CA, USA), with body temperature maintained at 37°C using forced heated air. A quadrature volume radiofrequency coil was used to scan the head region of mice. Axial T2-weighted images were acquired by using a fast spin-echo sequence with the following parameters: repetition time (TR)/effective echo time (TE), 4000/60 ms; echo spacing, 15 ms; number of echoes, 8; field of view, 20 × 20 mm; matrix, 256 × 128; slice thickness, 0.5 mm; number of slices, 25; and number of scans, 1 (Tscan time, 4.5 min). In addition, T1-weighted spin-echo images were acquired pre- and postgadolinium contrast injection by using the same slice package as above and with a TR/TE of 600/17 ms and an acquisition time of ~2.5 min. Finally, T2*-weighted gradient echo images were acquired by using the same slice package as above and with a TR/TE of 300/6 ms and an acquisition time of ~2.5 min. Tracer leakage studies were performed by intraperitoneal injection of 0.1 ml gadolinium-diethylenetriaminepentacetate (Gd-DTPA; 0.5 mM gadolinium-diethylenetriamine pentaacetic acid/ml; BioPAL, Worchester, MA, USA). Mice were active for 10 min before postinjection imaging.

Fusion proteins

Expression constructs used were as follows: Cx43, ZO-1, and Claudin-5 open reading frames were cloned into pmCherry-C1 vector and pAcGFP-C1 infusion ready vector (Clontech, Mountain View, CA, USA) to create N-terminally fused fluorescent proteins. Plasmid DNA was isolated from individual transformed Stellar Competent (TakaraBio, Mountain View, CA, USA) colonies by using Qiagen plasmid midiprep kits (Qiagen, Wetzlar, Germany). Open reading frame sequences were validated with Sanger sequencing. mBECs were transfected by using Torpedo^{DNA} (Ibidi, Fitchburg, WI, USA).

Inhibition studies

Inhibition of Cx43 GJs and HCs was achieved by cell treatment with 100 μM GAP27 (Cx43 gap junction and hemichannel inhibitor) or 100 μM GAP19 (Cx43 hemichannel inhibitor; Tocris Biosciences, Bristol, United Kingdom), respectively, for 24 h. Treatment did not affect cell viability as tested by Live Dead assay (Thermo Fisher Scientific). To inhibit vesicular transport and trancellular permeability, cells were pretreated with 0.1 mM

N-ethylmaleimide (Sigma-Aldrich) for 1 h and during the *in vitro* permeability assay.

Histology and immunofluorescence

Hematoxylin and eosin and Prussian blue staining was performed with frozen brain sections using standard procedures. Lesion stage classification was performed according to criteria described previously (5). In brief, stage 1 lesions are singular, dilated caverns that exhibit hemorrhage. Stage 2 lesions have segmented caverns with robust, prolonged hemorrhage. We introduce stage 0 lesions as dilated vessels with little or no hemorrhage.

Immunofluorescence staining of brain slices or cells was performed as described previously (4). Primary Abs used were as follows: Cx43 (Cell Signaling Technology, Danvers, MA, USA); ZO-1–Alexa Fluor 594, Claudin-5 unconjugated or Claudin-5–Alexa Fluor 488 (Thermo Fisher Scientific); and CD31/PECAM-1 (Novus Biologicals, Littleton, CO, USA). Secondary Abs used were as follows: FITC anti-rabbit and Texas Red anti-mouse (Vector Laboratories, Burlingame, CA, USA). Images were acquired on the Nikon A-1 confocal microscope (Nikon, Tokyo, Japan).

Quantitation of plaque size and TJ-associated fragments for Cx43, ZO-1, and Claudin-5 were performed using ImageJ software (National Institutes of Health, Bethesda, MD, USA). Three image fields per group with equal cell number were analyzed.

Cx43 expression in the capillaries of control ($ccm3^{+/-}p53^{+/-}$) mice or lesions of fCCM3 mice was quantified in ImageJ software by measuring fluorescence intensity of the entire endothelial region that surrounds the control vessel or lesion. Background fluorescence was subtracted from both control vessel and lesion fluorescence readings. Individual lesions (10 lesions) for stage 0 and 1, 2 individual stage 2 lesions, and 10 control vessels were analyzed from 3 control and 3 fCCM3 mice.

Super-resolution imaging

Super-resolution imaging was conducted in conjunction with the Single Molecule Analysis in Real-Time Center at the University of Michigan (Ann Arbor, MI, USA). Cells were plated at confluency in LabTek II Coverglass slides (0.17 mm thickness; Thermo Fisher Scientific). The following primary and secondary Abs were used: Cx43, Claudin-5, ZO-1–Alexa Fluor 647, goat anti-rabbit IgG Alexa Fluor Plus 647, and goat anti-mouse IgG Alexa Fluor Plus 647 (Thermo Fisher Scientific). Immediately before imaging, sample buffer was exchanged with STORM imaging buffer (100 mM Tris-Cl, 25 μM NaCl, 1% v/v 2-ME, pH 9.0) and freshly added 2.5 mM PCA (3,4-dihydroxybenzoic acid; P5630; Sigma-Aldrich) and 25 nM PCD (protocatechuate dioxygenase; P8279; Sigma-Aldrich). Images were collected in highly inclined laminated optical sheet microscopy illumination with 641-nm laser excitation on an Olympus IX81 microscope with a cell^TIRF module (Olympus, Tokyo, Japan). Images were collected on an Andor iXon Ultra EMCCD camera. Images were processed by using the ThunderSTORM plugin of ImageJ.

Quantitative PCR

Qunatitative PCR was performed after Trizol/chloroform RNA extraction and reverse transcription (SuperScript II RT; Thermo Fisher Scientific). Reactions were performed with SYBR Green PCR Master Mix and analyzed with 7500 Real-Time PCR System (Applied Biosystems, Foster City, CA, USA). Primers used were as follows: Cx37: forward: 5′-CTGGACCATGGAGCCGGTGT-3′, reverse: 5′-GGTTGAGCACCAGGGAGATGACTC-3′; Cx40: forward: 5′-TCCAGGGCACCCTACTCAACACCT-3′, reverse: 5′-GGACTCCTGCGGCAGACATGC; Cx43-3′: forward: 5′-TACCACGCCACCACCGGCCCA-3′, reverse: 5′-GGCATTTTGGCTGTCGTCAGGGAA-3′; and β-actin: forward: 5′-GCCCTGAGGCTCTTTTCCAG-3′, reverse: 5′-TGCCACAGGATTCCATACCC-3′ (n = 3 per group, normalized to β-actin expression). $\Delta\Delta C_t$ values were calculated, and fold-change reported.

Western blotting

Primary Abs used were as follows: Cx37 (Abcam, Cambridge, MA, USA); Cx40 (GeneTex, Irvine, CA, USA); Cx43 and β--tubulin; CCM1 (Boster Bio, Pleasanton, CA, USA); CCM2 (Sigma-Aldrich); CCM3 (ProteinTech, Rosemont, IL, USA); and ZO-1 and Claudin-5 (Thermo Fisher Scientific). Reactions were visualized with the following secondary Abs: goat anti-rabbit IgG-horseradish peroxidase conjugate or goat anti-mouse IgG-horseradish peroxidase conjugate (Bio-Rad, Hercules, CA, USA). Blots were developed with SuperSignal West Femto Maximum Sensitivity Substrate (Thermo Fisher Scientific) and imaged using the Molecular Imager ChemiDoc XRS+ Imaging System (Bio-Rad). Band intensities were analyzed by using Image Lab software (Bio-Rad).

GJ activity assays

Scratch assay was performed as follows: cells were grown to confluency before siRNA treatment. After media removal, the cell monolayer was disrupted with a single scratch. Lucifer yellow (LY; 0.05%; Sigma-Aldrich) was immediately applied to the scratch for 30 s. Cells were subsequently washed with PBS, fixed with 4% paraformaldehyde for 10 min, then immediately imaged by using a 488-nm laser line. Cell confluency that surrounded the scratch was confirmed under transmitted light. LY transfer distance was measured perpendicularly from scratch to the furthest LY^+ cell using ImageJ. Three independent scratches with 10 distance measurements per scratch were analyzed per group.

Microinjections were performed by using the PicoSpritzer 3 (Parker Hannifin, Richland, MI, USA). Cells were grown on Ibidi 35-mm low, grid 500, ibiTreat plates. Cell-of-origin grid location was recorded. Eppendorf Femptotips Microinjection capillary tips (0.5 μm; Thermo Fisher Scientific) were loaded with 0.05% LY. Healthy, confluent cells were injected at 40 kPa for 500 ms. LY injection was visualized in real time to ensure LY injection into the cell of origin. Three injections were performed at distant spots on each plate. After injection, cells were washed in PBS, fixed using 4% paraformaldehyde, and imaged immediately. LY^+ cells that surrounded the cell of origin were counted by using ImageJ.

Fluorescence resonance energy transfer and fluorescence recovery after photobleaching analysis

Fluorescence resonance energy transfer (FRET) and fluorescence recovery after photobleaching (FRAP) experiments were performed by using a Leica SP5X inverted 2-photon FLIM confocal microscope with LAS X software (Leica, Mannheim, Germany) at the University of Michigan Microscopy Imaging Laboratories. Laser power and line intensities used were as follows: FRET: white light laser, 70%; red laser line, 587 nm; 40% intensity; green laser line, 488 nm; 30% intensity; acceptor photobleaching performed with laser lines at 579, 587, and 595 nm at 100% for 80 s; FRAP: argon laser, 25%; green laser line, 488 nm; 30% intensity; photobleaching performed with 488 nm at 100%. Laser power and laser line intensities were kept constant across samples.

Experimental values were calculated as follows: FRET efficiency = [(donor^{post} − donor^{pre})/donor^{post}]; FRAP, % recovery = [(6 min postbleach fluorescence − 0 min post bleach fluorescence)/prebleach fluorescence] × 100.

Background controls used for FRET and FRAP experiments were as follows: FRET: background efficiency = FRET efficiency of coexpressed empty AcGFP and mCherry vectors subtracted from experimental FRET efficiencies during analysis; FRAP: a background region of interest (ROI) was selected in non-GFP$^+$ region. Background ROI percent recovery was subtracted from the experimental ROIs analyzed.

Transendothelial electrical resistance assay

Cells were grown to confluency in 12-mm Transwells with 0.4-μm pores (Corning, Corning, NY, USA) before manipulation. Transendothelial electrical resistance (TEER) values were measured by using the EVOM^2 Epithelial Voltohmmeter (World Precision Instruments, Sarasota, FL, USA). Blank measurements—media only, no cells—were subtracted from experimental values during analysis.

In vitro permeability assay

mBEC monolayers were established in the 12-mm Transwell system with 0.4-μm pore size. Permeability experiments were initiated with the addition of FITC-inulin (Sigma-Aldrich) to the apical (donor) chamber. The permeability coefficient (centimeters per minute) of the monolayer during any time interval (T) was calculated as follows:

$$PC = \frac{[C(B)_T - C(B)] \cdot V(B) \cdot 2}{[C(A) + C(A)_T] \cdot A \cdot T},$$

where $C(B)$ and $C(B)_T$ are the concentrations (nanograms per milliliter) of FITC-inulin in the basal (receiving) chamber at the start and at the end of the time interval, respectively, and $V(B)$ is the volume of the basal chamber (in milliliters). $C(A)$ and $C(A)_T$ are the concentrations of FITC-inulin in the apical (donor) chamber at the start and at the end of the time interval, respectively, and $[C(A) + C(A)_T]/2$ is the average concentration over the time interval. T is the duration of the time interval (in minutes), whereas A is the area of the filter (square centimeters). All samples were read on a fluorescent reader (Infinity FL200; Tecam, Saint Charles, IL, USA). The concentration of FITC-inulin in samples was calculated from a standard curve that was derived using known concentrations of tracer (4, 14, 15).

For transcellular permeability, the percentage of cellular uptake of FITC-albumin was evaluated at 37°C by adding FITC-albumin (1 mg/ml) and in the presence or absence of unlabeled albumin. Uptake at 37°C was allowed to proceed for time points 0–120 min (15-min interval), then terminated by chilling on ice and washing 3 times with PBS buffer. Cell-surface binding of FITC-albumin was removed by 0.5 ml acid buffer (0.5 M NaCl and 0.2 M acetic acid, pH 2.5). Cells were lysed with 0.5 ml of 50 mM Tris HCl, pH 7.4, that contained 1% Triton X-100 and 0.5% SDS, and the sample was read on a fluorescent reader (15).

Statistical analyses

Statistical analyses were performed by using Prism 6.0 (GraphPad Software, La Jolla, CA, USA). Data in bar graphs represent means ± SEM. In experiments that compared 2 groups, significant differences were determined by unpaired, 2-tailed Student's t test. In experiments that compared >2 groups, significant differences were determined by a 1-way ANOVA with Tukey's *post hoc* test. A probability value of $P < 0.05$ was considered statistically significant.

RESULTS

GJ protein, Cx43, is elevated in an fCCM3 mouse model

To study the role of Cx43 in fCCM3, we bred a mouse model of fCCM3 [$ccm3^{+/-}p53^{-/-}$ mice, described previously (6)] on the basis of the 2-hit hypothesis of fCCM in which a second somatic mutation is acquired in the functional allele of heterozygous patients (12). fCCM mouse models on $p53^{-/-}$ backgrounds develop cerebrovascular hemorrhagic lesions. Additional organ pathologies were not detected (6). $ccm3^{+/-}p53^{-/-}$ mice were evaluated for the presence of hemorrhagic cerebrovascular lesions that were consistent with human disease by using T2*-weighted MRI imaging. Several hemorrhagic lesions were present in multiple regions of the brain at age 5 wk (**Fig. 1*A***). Lesion volume varied between 0.005 and 1.0 mm^3. New hemorrhagic lesions appeared at a rate of 3–4.5 lesions per week (data not shown).

Given that BBB hyperpermeability is the central pathologic feature of fCCM3, lesion permeability in the $ccm3^{+/-}p53^{-/-}$ model was evaluated by using Gd-DTPA injection. Gd-DTPA leakage could frequently be observed in conjunction with hemorrhage on companion T2*-weighted MRI images. Lesions were categorized into 2 types: permeable (Gd-DTPA leakage only, nonhemorrhagic) and hemorrhagic (Fig. 1*B*). When first assessed at age 9 wk, $ccm3^{+/-}p53^{-/-}$ mice had roughly equivalent numbers of permeable and hemorrhagic lesions. Hemorrhagic lesions were most prevalent by age 13 wk (Fig. 1*B*). When individual permeable lesions at age 9 wk were followed to age 13 wk, the probability of lesion hemorrhage was 100% (data not shown). These findings demonstrate that developing lesions have compromised BBB function before hemorrhage. Of importance, lesion permeability predicts hemorrhage. Histologic examination of lesion maturation in hematoxylin and eosin–stained sections revealed stage 0, 1, and 2 lesions, classified as described in Materials and Methods (Fig. 1*C, D*). Evaluation of prolonged hemorrhage by iron accumulation using Prussian blue staining revealed iron accumulation in stage 1 and 2 lesions. Overall, lesion maturation progresses from a permeable dilated vessel (stage 0) to reorganized, cystic-like caverns with a complete loss of barrier properties and hemorrhage (stages 1 and 2).

We sought to identify proteins that are aberrantly expressed in stage 0 lesions that promote BBB hyperpermeability and enable lesion maturation. Aberrant elevation of Cx43 protein has recently been linked to increased barrier permeability (10, 11). Immunofluorescence staining of Cx43 in $ccm3^{+/-}p53^{-/-}$ lesions revealed dramatically increased Cx43 expression in all lesion stages, particularly at stage 0, which correlates with lesion progression (Pearson coefficient $r = 0.7074$; $P < 0.01$; Fig. 1*C, D*). The increased expression of Cx43 was observed in

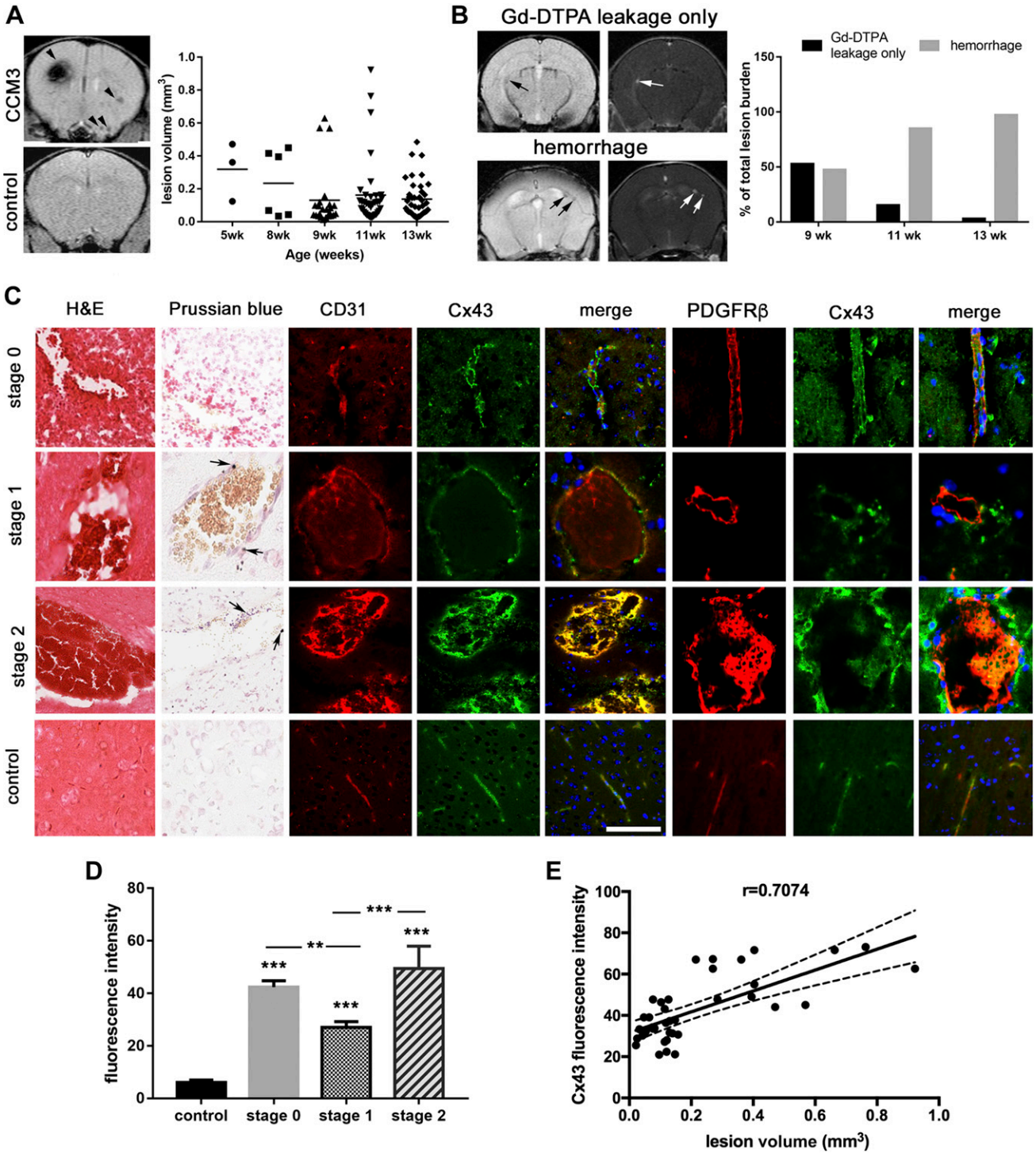

Figure 1. Developing lesions expressing Cx43 are susceptible to hemorrhage. *A*) T2* MRI images of a $ccm3^{+/-}p53^{-/-}$ mouse and $ccm3^{+/-}p53^{+/-}$ control mouse. Multiple hemorrhages of variable size are visible in the $ccm3^{+/-}p53^{-/-}$ mouse (black arrows). Compiled lesion volumes of 3 $ccm3^{+/-}p53^{-/-}$ mice assessed at age 5, 8, 9, 11, and 13 wk. *B*) Representative image of $ccm3^{+/-}p53^{-/-}$ mouse lesions with Gd-DTPA leakage only (top) and Gd-DTPA + hemorrhage (bottom) as assessed by T1-weighted (Gd-DTPA) or T2*-weighted (hemorrhage) imaging. The number of Gd-DTPA^{+} lesions with or without hemorrhage was counted at age 9, 11, and 13 wk and presented as a percent of the total number lesions identified in T1 or T2* images. *C*) Hematoxylin and eosin (panel 1), Prussian blue (panel 2, black arrows indicate spots of iron accumulation), and immunofluorescence staining of CD31 (panel 3), Cx43 (panel 4), merge images (panel 5), PDGFRβ (panel 6), Cx43 (panel 7) and merge images (panel 8) of stage 0, 1, and 2 lesions and control vessels in $ccm3^{+/-}p53^{-/-}$ mice. Scale bar, 100 μm. *D*) Quantitation of Cx43 expression in control and lesion stages ($n = 10$; $n = 10$ individual lesions for stage 0 and 1; $n = 2$ individual lesions for stage 2). Cx43 was quantified using ImageJ by selecting the entire endothelial layer surrounding each lesion and measuring the fluorescent signal. Cx43 expression is quantified relative to control vessel fluorescence. *E*) Comparison of Cx43 expression and lesion volume (Pearson coefficient $r = 0.7074$, $P < 0.01$). ***$P < 0.0001$ compared to control, **$P < 0.01$ compared with stage 0, ***$P < 0.001$ compared with stage 1.

brain endothelial cells ($CD31^+$) and surrounding pericytes (platelet-derived growth factor receptor β^+ cells; Fig. 1C). Given our observation that Cx43 is significantly elevated in permeable stage 0 lesions, Cx43 was pursued for additional study to identify its pathogenic functions in fCCM3.

Cx43 protein and GJ activity is increased by CCM3KD *in vitro*

We established an *in vitro* fCCM3 model by using CCM3KD in a mBEC line, achieving 85% efficiency of CCM3KD (Supplemental Fig. 1). Cx43 protein, but not transcript, is elevated in CCM3KD cells (**Fig. 2*A*, *B***). No difference in protein expression was observed for Cx37 and Cx40, additional Cx family members that are expressed by brain endothelial cells, although a compensatory up-regulation of Cx40 transcript was apparent (Fig. 2*A*, *B*). To determine whether Cx43 is elevated in other fCCM subtypes, Cx43 protein expression was analyzed in CCM1KD and CCM2KD cells, which revealed significant, but not robust, elevation compared with control cells (Supplemental Fig. 1).

Cx43 has many functions that are dependent on its cellular localization (16, 17). Cell fractionation analysis of Cx43 revealed that Cx43 is localized exclusively to the insoluble fraction in control cells, and CCM3KD does not change its cellular localization (Fig. 2*C*). Immunofluorescence staining of Cx43 confirmed that, in both control and CCM3KD cells, Cx43 was localized to the membrane and formed plaque-like structures that were consistent with GJ plaques (Fig. 2*E*). Quantitation of Cx43 GJ plaque size revealed significantly increased Cx43 GJ plaque size in CCM3KD cells compared with controls (Fig. 2*F*). FRAP analysis suggested that no difference in Cx43 mobility within GJ plaques exists between control and CCM3KD cells (Fig. 2*D*).

We evaluated whether enlarged Cx43 GJ plaques in CCM3KD cells have a functional effect on GJ intracellular communication (GJIC). Single-cell microinjection of LY, a noncell permeable dye, into control or CCM3KD cell monolayers demonstrated a significantly higher capacity for CCM3KD cells to transfer dye to adjacent cells than control cells (**Fig. 3*A***). Scratch assay analysis of LY transfer in control or CCM3KD cell monolayers also demonstrated significantly elevated GJIC in CCM3KD cells compared with controls. To validate that LY transfer occurred specifically *via* Cx43 GJs, and not Cx37 or Cx40 GJs, we performed scratch assays in the presence of a Cx43 GJ-specific peptide inhibitor, GAP27 (18). GAP27 completely inhibited CCM3KD GJIC, which indicated that Cx37 and Cx40 were not directly contributing to GJIC in CCM3KD cells. Morphologic analysis suggested that prolonged GAP27 treatment inhibited GJIC by decreasing GJ plaque size in CCM3KD cells (Fig. 3*B*). Super-resolution imaging highlighted the reduction in GJ plaque size (Fig. 3*C*).

Cx43 expression in $ccm3^{+/-}p53^{-/-}$ lesions suggests that elevated Cx43 is associated with permeability. To evaluate whether elevated Cx43 protein expression in CCM3KD cells contributes to hyperpermeability that is characteristic of fCCM3, we measured TEER and permeability (clearance) for tracer inulin in CCM3KD cells in which Cx43 protein expression was reduced *via* siRNA-mediated knockdown (**Fig. 4*A*, *B*** and Supplemental Fig. 2A). As expected, CCM3KD cells exhibited highly permeable monolayers, as did wild-type cells that overexpressed Cx43 ($Cx43^{over}$). Of importance, reducing Cx43 expression in CCM3KD cells partially, but significantly, restored the integrity of CCM3KD monolayers (Fig. 4*B*).

To test which function of Cx43 is pathologic to permeability, we examined whether the inhibition of Cx43 GJIC could rescue CCM3KD monolayer permeability (Fig. 4*C*). TEER analysis of control and CCM3KD cells in the presence of GAP27 or GAP19, a Cx43 HC-specific inhibitor (19), revealed that GAP27 completely rescued CCM3KD monolayer permeability, with no adverse effect on control cells, whereas GAP19 had no effect on CCM3KD TEER. This Cx43 effect on brain endothelial monolayer permeability was accomplished mostly by opening a paracellular route, whereas transcellular permeability, measured by transcellular transport of FITC-albumin, was affected to a modest degree (Fig. 4*D*).

Analysis of key occlusion (Claudin-5) and scaffolding (ZO-1) proteins indicated that CCM3KD and $Cx43^{over}$ cells exhibited reduced expression of both Claudin-5 and ZO-1 (**Fig. 5*A***), which suggested that elevated Cx43 protein expression may be pathologic to CCM3KD cells by regulating permeability with a TJ protein expression–dependent mechanism. As in CCM3KD and $Cx43^{over}$ cells, CCM3 lesions unveiled the same pattern of Claudin-5 and ZO-1 expression. Both TJ proteins demonstrated decreased expression in CCM3 lesions and negatively correlated with increased lesions (Claudin-5: $r = -0.8621$; ZO-1; $r = -0.8331$) and increased Cx43 expression (Claudin-5: $r = -0.726$; ZO-1: $r = -0.6201$; Fig. 5*B*, *C*).

Cx43 GJs disrupt TJ formation in CCM3KD cells

Having determined that Cx43 GJIC is pathologic to CCM3KD permeability, we next examined how Cx43 GJs regulate permeability in CCM3KD cells. ZO-1 emerged as a candidate protein that links Cx43 to permeability because of a well-described Cx43–ZO-1 interaction (20). The Cx43–ZO-1 interaction restricts Cx43 GJ size (21–23); however, whether Cx43 GJs can regulate ZO-1, particularly its function in TJs, is unknown. We tested the hypothesis that Cx43 GJs affect the organization of TJs *via* regulating ZO-1 localization. Immunofluorescence analysis of Cx43 and ZO-1 colocalization in control, CCM3KD, and GAP27-treated CCM3KD cells revealed significant differences in the TJ association (continuous cell border staining) and GJ association (Cx43–ZO-1 colocalization) of ZO-1 (**Fig. 6*A***). ZO-1 in control cells exhibits preferential localization to TJs and low accumulation at GJs. In contrast, ZO-1 in CCM3KD cells exhibited fragmented localization to TJs and aberrant accumulation at GJs (Fig. 6*B*, *C*). Comb-like ZO-1 structures that extend into the cytosol from the cell border, characteristic of disorganized ZO-1, were observed in super-resolution imaging of ZO-1 in CCM3KD cells (Fig. 6*D*). Of interest, inhibition of Cx43 GJIC in CCM3KD cells with GAP27 partially restored the

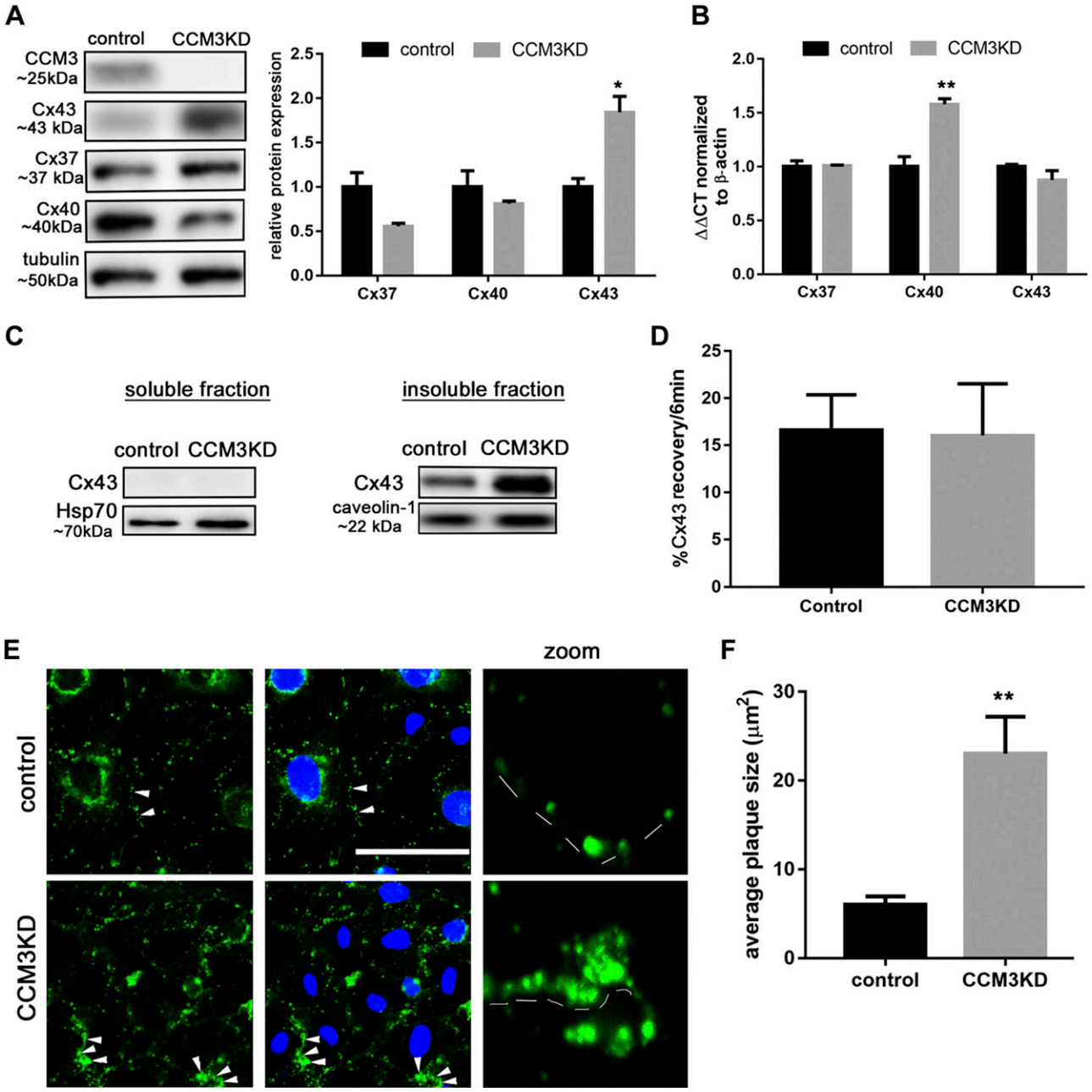

Figure 2. Cx43 protein is increased in CCM3KD brain endothelial cells. *A*) Control or CCM3KD (siRNA-mediated 85% CCM3 knockdown; Supplemental Fig. 1) whole-cell lysates were prepared and analyzed *via* Western blot. Cx43 protein, but not Cx37 or Cx40 protein, is significantly elevated relative to control ($n = 3$ independent experiments). *$P < 0.05$ compared to control. *B*) RNA extracted from control and CCM3KD cells and subjected to reverse-transcription quantitative PCR revealed no significant changes in Cx43 transcript. Data represent means ± SEM fold-change normalized to β-actin (Cx43: $n = 6$, Cx40, Cx37: $n = 3$ independent experiments). **$P < 0.01$ compared with control. *C*) Whole-cell lysates were subjected to cell fractionation. Cx43 was only present in the insoluble fraction (caveolin-1) and not in the cytosol (Hsp70; representative Western blot, $n = 3$ independent experiments). *D*) FRAP analysis of control and CCM3KD cells expressing Cx43-AcGFP. FRAP was performed on membrane ROIs ($n = 6$ ROIs from 6 cells). *E*) Immunofluorescence staining of Cx43 (column 1), merged Cx43, and DAPI staining (column 2), and zoom images of Cx43 GJs along the cell membrane (column 3, dashed lines) in control and CCM3KD cells (GJ plaques are indicated with white arrows). Scale bar, 100 μm. *F*) Cx43 GJ plaque size was measured in ImageJ. For 3 image fields with ~8 cells/field, the entire membrane region of every cell was selected to analyze particle (GJ plaque) size in Cx43-labeled samples. Average plaque size is reported as mean ± SEM of all GJ plaques measured (~50 plaques/field). This analysis revealed significantly larger GJ plaques in CCM3KD cells compared with controls. **$P < 0.01$.

localization of ZO-1 to TJs and prevented the accumulation at GJs.

We analyzed the mobility of TJ-associated ZO-1 with FRAP (Fig. 6*E*). Given its size and function as a scaffolding protein, ZO-1 is a relatively immobile protein in healthy cells. We determined that ZO-1 is significantly more mobile in CCM3KD cells compared with controls, which supports our finding that ZO-1 is not sufficiently anchored

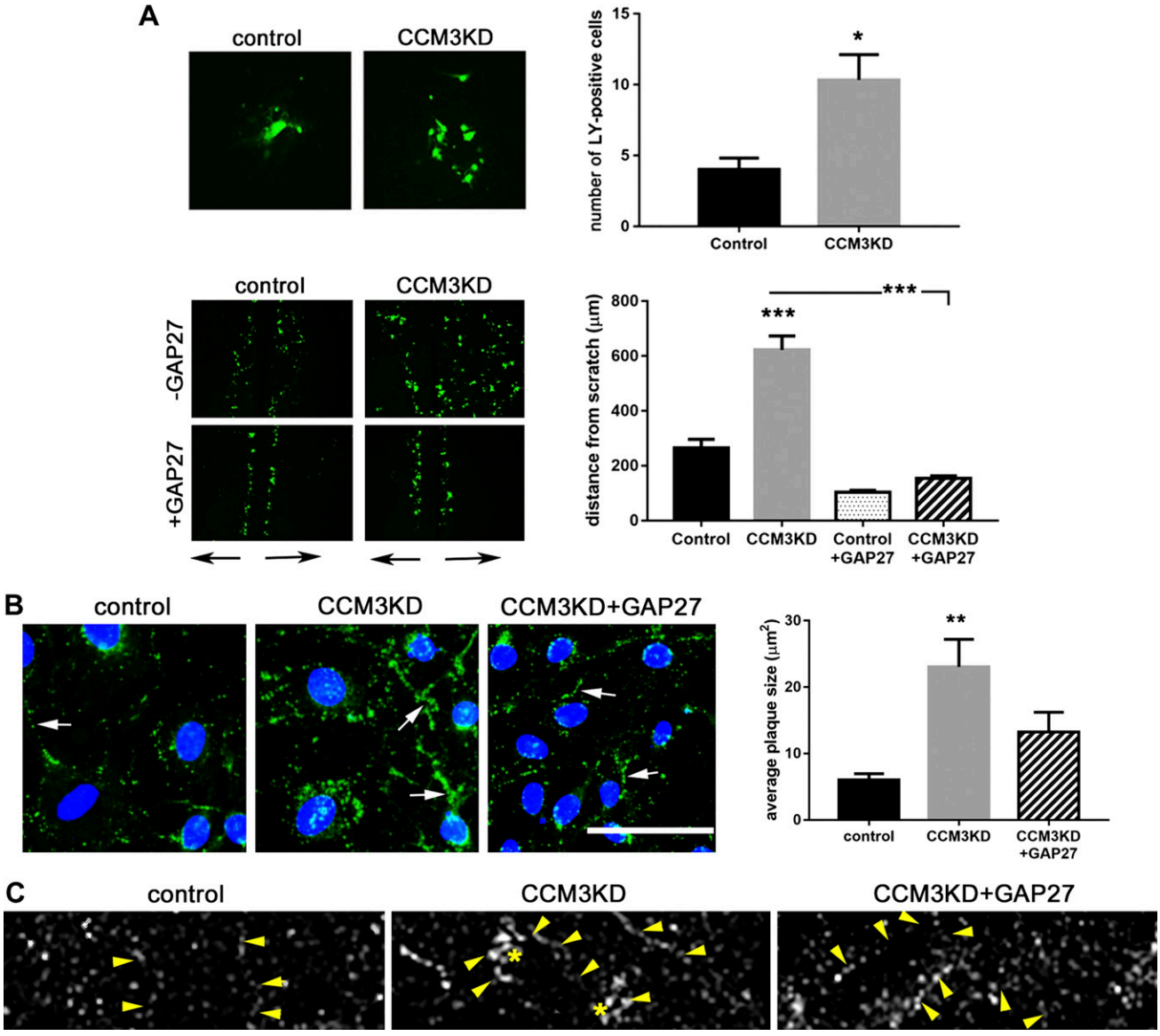

Figure 3. CCM3KD cells have increased GJIC. *A*) GJIC measured by microinjection (top) and scratch assay (bottom). Single-cell injections were performed in control and CCM3KD samples. The number of neighboring LY^+ cells was counted in ImageJ ($n = 3$ independent injections over 3 plates). $^*P < 0.05$. Scratch assays also revealed a significant increase in GJIC function as measured by the distance of LY spreading perpendicular to the scratch (black arrows below image) in CCM3KD cells compared with controls. GJIC could be rescued by treatment with 100 μm GAP27 for 24 h. Magnification, ×4. Data represent means ± SEM ($n = 3$ independent experiments, 10 measurements/experiment). $^{***}P < 0.0001$ compared with control or CCM3KD. *B*) Immunofluorescence staining of Cx43 GJ plaques (white arrows) in control, CCM3KD, and CCM3KD + GAP27 reveals the rescue of plaque size by 100 μM GAP27 treatment for 24 h. Scale bar, 100 μm. Plaque size was quantified in ImageJ as described in Fig. 2*F* ($n = 3$ image fields, ~50 plaques/field). $^{**}P < 0.01$ compared with control. *C*) Super-resolution imaging of control, CCM3KD, and CCM3KD cells treated with 100 μM GAP27 for 24 h. Arrows indicate cell border, stars indicate GJ plaques.

in TJ structures. GAP27 treatment restores ZO-1 mobility to control levels, which is also consistent with the redistribution of ZO-1 to TJ structures in GAP27-treated CCM3KD cells.

To further delineate the nature of Cx43–ZO-1 colocalization that was observed in CCM3KD cells, we used acceptor-photobleaching FRET analysis in cells that coexpressed Cx43-mCherry and ZO-1–AcGFP. FRET efficiency between Cx43 and ZO-1 in CCM3KD cells was significantly lower compared with controls (Fig. 6*F*), which indicated that whereas Cx43 and ZO-1 strongly colocalize in CCM3KD cells, they do not physically interact to the same extent as in control cells. This is consistent with our data that indicate higher GJ activity and the literature that shows that Cx43–ZO-1 interaction inhibits GJIC. Finally, GAP27 treatment of CCM3KD cells restores the Cx43–ZO-1 interaction, which is consistent with the inhibition of GJIC and further supports the notion that the Cx43–ZO-1 interaction is important for Cx43-mediated effects on permeability.

We extended our analysis of Cx43 GJ-mediated regulation of TJs to include the TJ transmembrane protein, Claudin-5. Similar to ZO-1, we observed that Claudin-5 is more mobile in CCM3KD cells compared with controls.

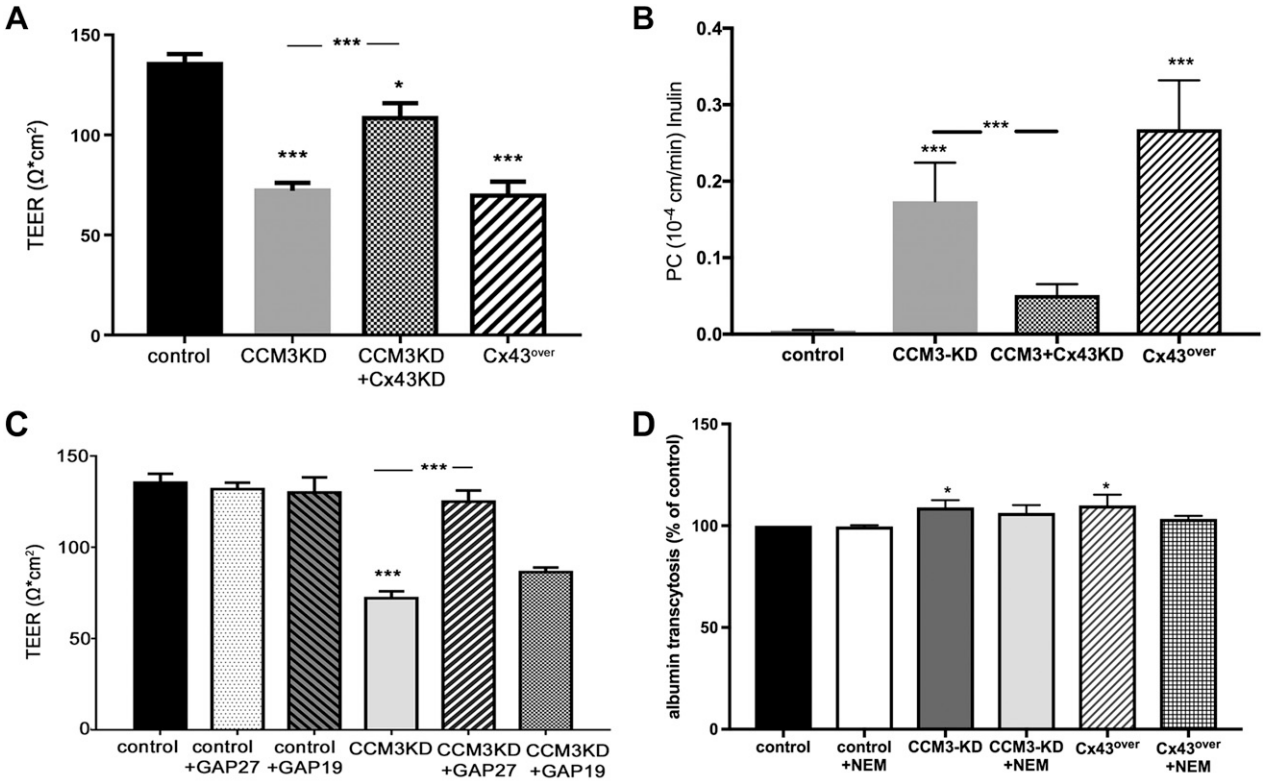

Figure 4. Depletion of Cx43 protein and GAP27-mediated inhibition of Cx43 GJIC rescues CCM3KD monolayer permeability. *A*) Transwell TEER assays revealed a significant increase in CCM3KD permeability and partial, significant rescue after the reduction of Cx43 expression in CCM3KD cells *via* Cx43 siRNA-mediated KD. Data represent means ± SEM (n = 3–10 independent experiments). $^*P < 0.05$, $^{***}P < 0.0001$ compared with control, $^{***}P < 0.001$ compared with CCM3KD. Cx43 + CCM3KD efficiency is reported in Supplemental Fig. 2. *B*) Permeability coefficient (PC) of inulin (MW = 5 kDa) shows increased permeability of CCM3KD and Cx43^{over} mBEC monolayers, whereas the depletion of Cx43 *via* siRNA rescued mBEC monolayer integrity. Data represent means ± SEM. $^{***}P < 0.001$ compared with control, $^{***}P < 0.001$ compared with CCM3KD. *C*) Transwell TEER assays performed with control and CCM3KD cells treated with 100 μm GAP19 or 100 μM GAP27 for 24 h. Treatment with GAP27 completely rescued CCM3KD permeability. GAP19 treatment had no effect (n = 3–10 independent experiments). $^{***}P < 0.0001$ compared with control or CCM3KD. *D*) Transendothelial albumin permeability was only slightly increased in CCM3KD and Cx43^{over} monolayers compared with control. Inhibition of vesicular transport with *N*-ethylmaleimide (NEM) did not disturb the albumin monolayer permeability, which indicated that CCM3 and Cx43 predominantly regulate paracellular permeability. Data represent means ± SEM. $^*P < 0.05$ compared with control.

This trend was rescued by GAP27 treatment (**Fig. 7*A***). Super-resolution imaging of Claudin-5 demonstrated continuous staining of Claudin-5 along the cell border in control cells, which was indicative of TJ incorporation (Fig. 7*B*). As with ZO-1, TJ-incorporated Claudin-5 seems to be fragmented in CCM3KD cells, but GAP27-mediated inhibition of Cx43 GJIC restored the localization of Claudin-5 to TJs. Examination of ZO-1–Claudin-5 colocalization, a necessary step for the formation of functional TJs (23), indicated expected colocalization at TJ structures along the cell border in control cells, but fragmented TJ-associated Claudin-5 in CCM3KD cells (Fig. 6*C*). Quantitation of TJ-associated Claudin-5 fragment length revealed highly fragmented TJ-associated Claudin-5 in CCM3KD cells, but rescued TJ-associated fragment length by inhibition of Cx43 GJIC with GAP27. Finally, we analyzed the frequency of Claudin-5–ZO-1 and Claudin-5–Claudin-5 transinteractions with FRET (Fig. 7*D, E*). TJ-associated Claudin-5 and ZO-1 interacted less frequently in CCM3KD cells, but this interaction was restored by Cx43 GJIC inhibition. Similarly, Claudin-5–Claudin-5 transinteraction was compromised in CCM3KD cells, but restored by the GAP27-mediated inhibition of Cx43 GJIC.

DISCUSSION

Hyperpermeability is the primary defect of fCCM3 lesions; however, the underlying mechanism that contributes to hyperpermeability is not well defined. The present study observed that 1) Cx43 forms large GJ plaques and displays increased GJIC in CCM3KD cells; 2) the inhibition of Cx43 GJIC completely rescued CCM3KD hyperpermeability; 3) Cx43 GJs regulated permeability *via* modulating TJ protein localization; and 4) Cx43 protein expression in lesions of $ccm3^{+/-}p53^{-/-}$ mice was elevated.

Permeability of the brain microvascular system is regulated, in part, by the TJ complex. The formation of TJ structures on the membrane is a highly regulated, multistep process. ZO-1 is recruited and distributed along the cell border, which signals the recruitment and insertion of claudins and occludin into the membrane, which in turn,

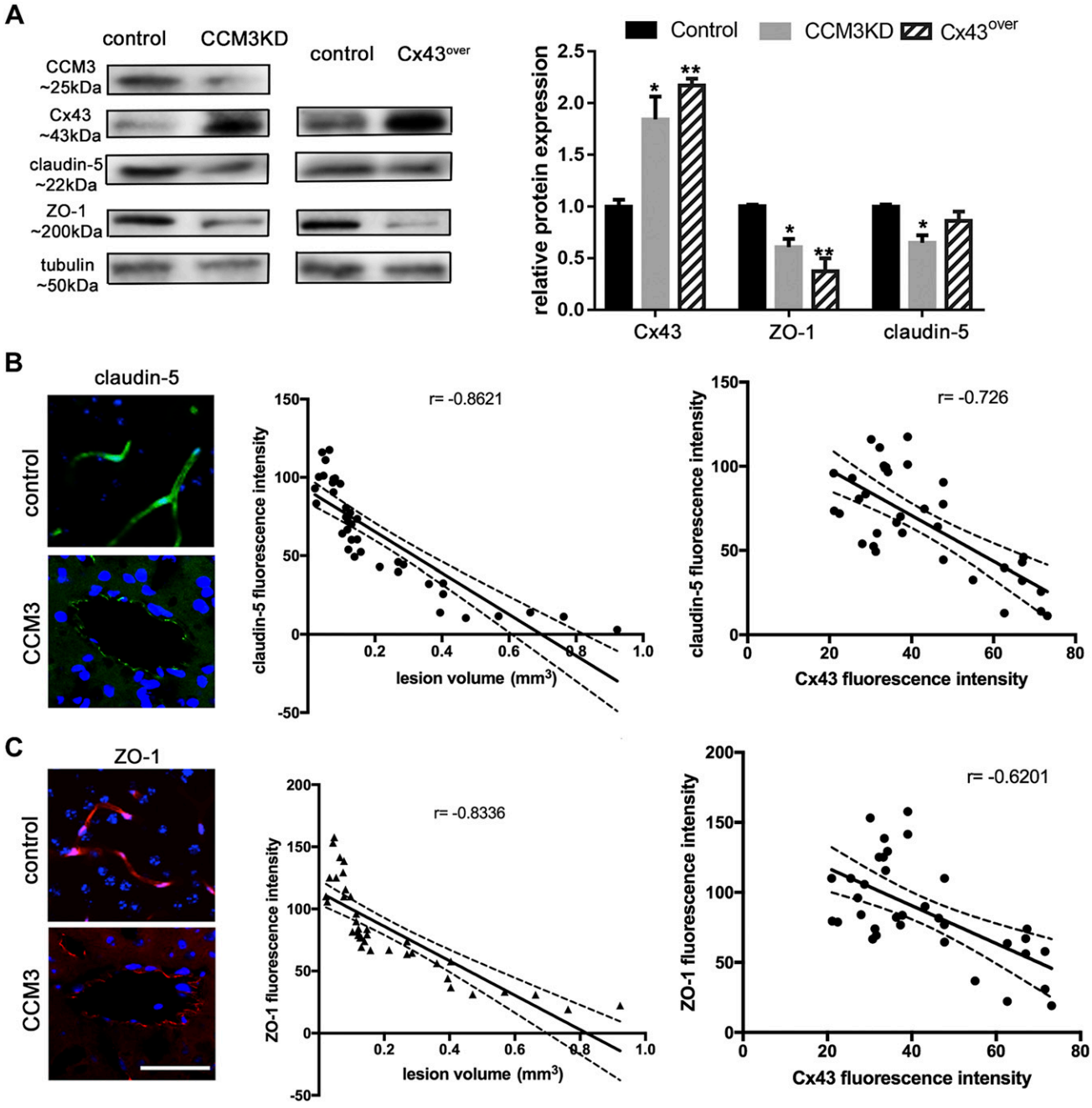

Figure 5. *A*) Representative Western blot and quantification of Cx43, Claudin-5, and ZO-1 in whole-cell lysates of control, CCM3KD, and Cx43 overexpressing ($Cx43^{over}$) cells ($n = 3$ independent experiments). Cx43: $^{*}P < 0.05$, $^{**}P < 0.01$ compared with control; ZO1: $^{*}P < 0.05$, $^{**}P < 0.01$ compared with control; Claudin-5: $^{*}P < 0.05$ compared with control. *B, C*) Immunofluorescence staining for Claudin-5 (*B*) and ZO-1 (*C*) in control and CCM3 lesion stage 1 unveiled decreased Claudin-5 expression. Correlation between Claudin-5/ZO-1 expression and lesion volume (Pearson coefficient: Claudin-5: $r = -0.8621$; $^{***}P < 0.001$; and ZO-1: $r = -0.8336$, $^{***}P < 0.001$) and Claudin-5/ZO-1 and Cx43 expression in CCM3 lesion (claudin-5: $r = -0.726$ $^{***}P < 0.001$; and ZO-1: $r = -0.601$, $^{***}P < 0.001$). Scale bar, 100 μm.

allows transinteractions between claudins and occludin on neighboring cells (23). Claudin-5 is a particularly crucial claudin for BBB occlusion. Claudin-5 knockout mice die hours after birth from brain edema as a result of inhibited BBB occlusion (24). Other claudin KO mice suggest that Claudin-5 is uniquely important for barrier occlusion (25). Previous works have demonstrated that fCCM3 lesions have highly disorganized TJ structures, including absent or incomplete incorporation of ZO-1 and Claudin-5 into TJs, and suggest that this is a principal mechanism by which fCCM3 lesions are hyperpermeable (4); however, the underlying mechanism that contributes to TJ organization has not been defined.

Elevated Cx43 has recently been suggested to be detrimental to barrier permeability in GJ- and HC-dependent mechanisms. Multiple studies in lung endothelia have

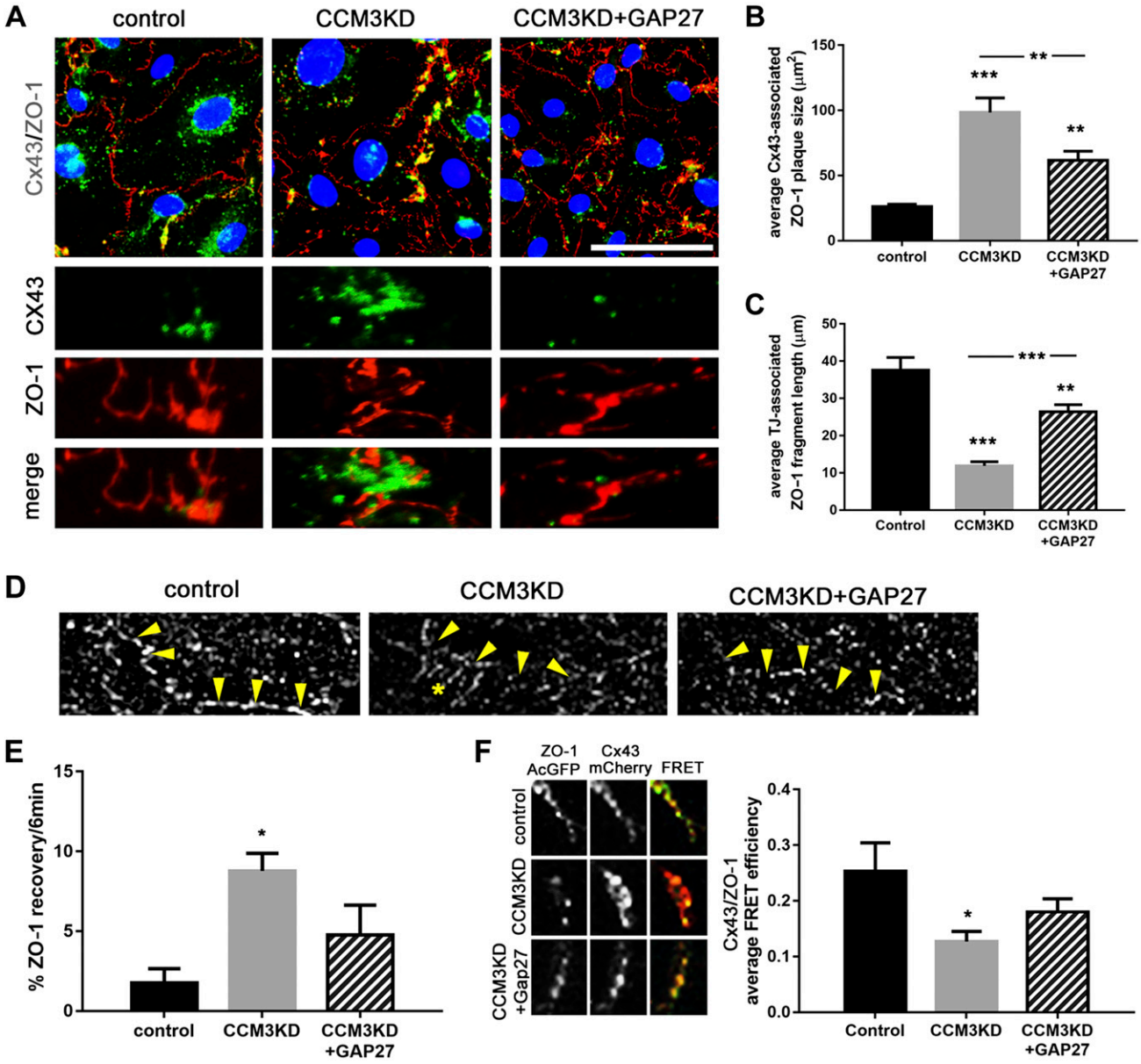

Figure 6. Inhibition of Cx43 GJIC rescues TJ disorganization in CCM3KD cells. *A*) Immunofluorescence staining of Cx43 and ZO-1 in control, CCM3KD, and CCM3KD + GAP27 (100 μm) cells. Zoom images demonstrate Cx43 GJ-plaque associated ZO-1 and TJ-associated ZO-1, represented by continuous staining along the cell border. Scale bar, 100 μm. *B*) Quantitation of Cx43 GJ-associated ZO-1 plaque size was performed in ImageJ by measuring individual ZO-1 plaques associated with Cx43 as determined by corresponding Cx43–ZO-1 merged images. Three image fields with ~8 cells/field, 15 plaques/field were analyzed. CCM3KD cells display significantly larger Cx43-associated ZO-1 plaques compared with control. GAP27 treatment of CCM3KD cells significantly reduced CCM3KD ZO-1 plaques. $***P < 0.0001$, $**P < 0.01$ compared with control, $**P < 0.01$ compared with CCM3KD. *C*) Quantitation of TJ-associated ZO-1 fragments along the cell border. The length of ZO-1 fragments along the cell border was measured for 3 image fields with 8 cells/field in ImageJ. $***P < 0.0001$, $**P < 0.01$ compared to control, $***P < 0.0001$ compared with CCM3KD. *D*) Super-resolution images of TJ-associated ZO-1 fragments on the cell border (arrows) and comb-like organization in CCM3KD cells (star). *E*) FRAP analysis of TJ-associated ZO-1 in control, CCM3KD, and CCM3KD+GAP27 cells expressing ZO-1-AcGFP. $*P < 0.05$ compared with control. *F*) Acceptor photobleaching FRET of Cx43 GJ-associated ZO-1 in cells coexpressing Cx43-mCherry and ZO-1-AcGFP in control, CCM3KD, or CCM3KD + GAP27 cells ($n = 30$ ROIs/group). $*P < 0.05$ compared with control.

demonstrated the rescue of barrier properties after suppression of inflammation-induced Cx43 expression (11, 26). In brain endothelia, elevated GJIC is suggested to be pathogenic to barrier function because of the effects of Ca^{2+} propagation on cytoskeletal integrity or localized endothelial cell death (27, 28). Cx43 has not previously been evaluated in fCCM. We observed robust expression of Cx43 in all stages of lesions in $ccm3^{+/-}p53^{-/-}$ mice, with particularly high expression in developing stage 0 lesions. Brain endothelial cells that were subjected to CCM3KD also demonstrated high protein expression of Cx43 and formed abnormally large GJ plaques that resulted in

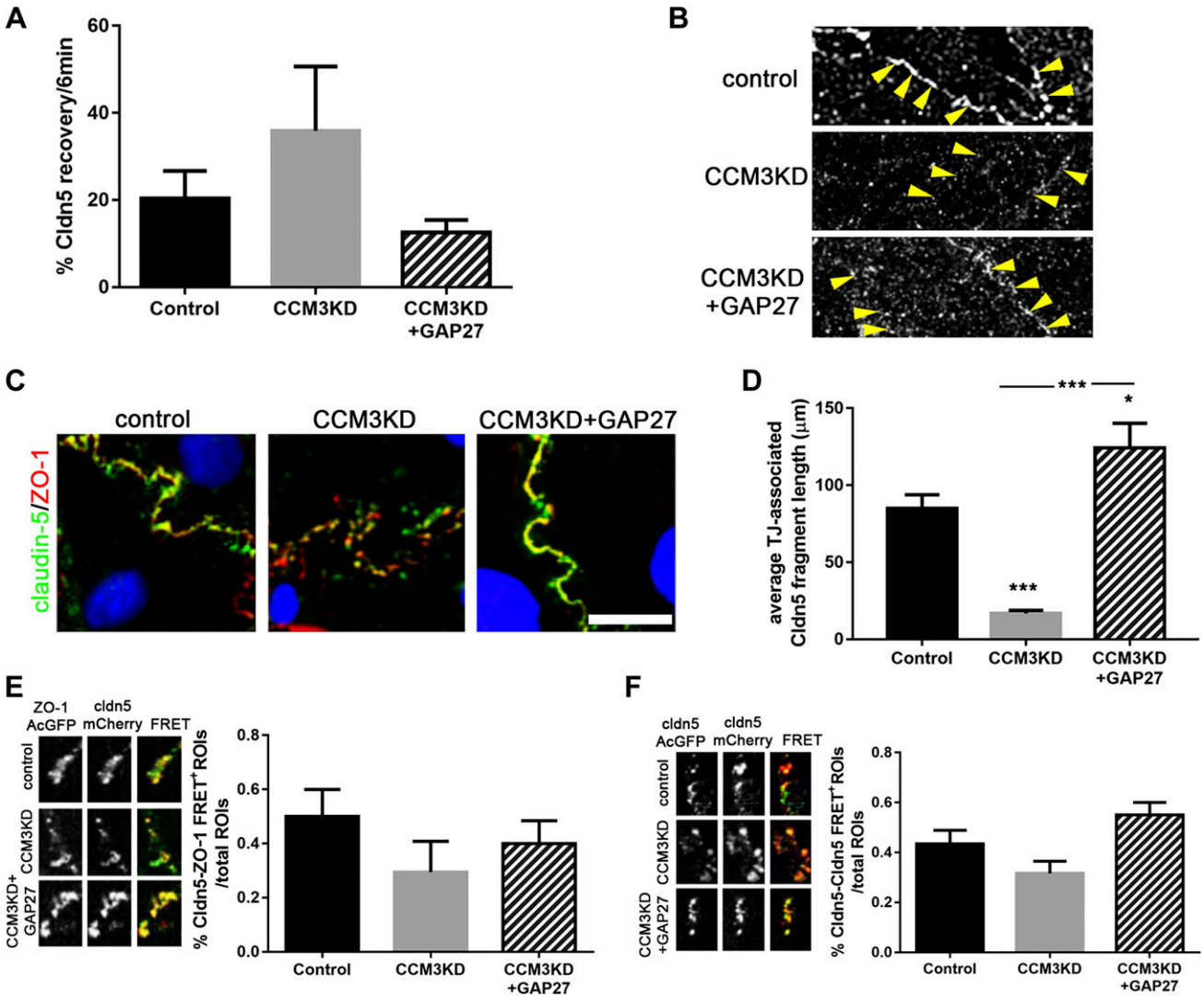

Figure 7. Claudin-5 incorporation into TJs is rescued by Cx43 GJ inhibition. *A*) FRAP analysis of Claudin-5 (Cldn5) in control, CCM3KD, and CCM3KD + GAP27 (100 μm) cells expressing Claudin-5–AcGFP. *B*) Super-resolution imaging of TJ-associated Claudin-5 (arrows). *C*) Immunofluorescence staining of Claudin-5 and ZO-1 in control, CCM3KD, and CCM3KD + GAP27 (100 μM) cells. Scale bar, 25 μm. *D*) Quantitation of the average TJ-associated Claudin-5 fragment length in Claudin-5/ZO-1 costained immunofluorescent images. Fragment length was measured in ImageJ as described for ZO-1 fragment length in Fig. 5*C*. $*P < 0.05$, $***P < 0.0001$ compared with control, $***P < 0.0001$ compared with CCM3KD. *E*) FRET analysis of TJ-associated Claudin-5 and ZO-1 in cells coexpressing Claudin-5–mCherry and ZO-1–AcGFP. The number of cell-border ROIs giving a FRET signal ($FRET^+$ ROI) was measured as a percent of the total number of cell-border ROIs analyzed [$n = 20$ total ROIs (4 ROIs/cell), 2 independent experiments]. *F*) FRET analysis of Claudin-5 transinteraction. Cells were separately transfected with either Claudin-5–AcGFP or Claudin-5–mCherry at 1:1 concentration, then seeded together. ROIs in which neighboring cells exhibited incorporation of Claudin-5–AcGFP and Claudin-5–mCherry into a shared TJ were selected for FRET analysis. FRET was performed and analyzed as described in Fig. 6*E* for 15 ROIs (3 ROIs/cell) and 2 independent experiments.

elevated GJIC. We found that reducing Cx43 expression and specific blockage of GJIC, but not HC function, rescued their hyperpermeability.

Understanding how elevated GJIC in fCCM3 causes hyperpermeability is of great importance. Here, we propose a mechanism that is separate from the aforementioned studies that examined Cx43-dependent hyperpermeability by which increased Cx43 GJs inhibit the distribution of ZO-1 and, consequently, Claudin-5 to the TJ. A large body of literature has described the interaction between Cx43 and ZO-1 in the context of GJ size and activity, in which the direct interaction of Cx43 and ZO-1 at the GJ plaque perimeter decreases GJ plaque size and activity (29, 30). We observed a phenomenon not yet described by which ZO-1 accumulates at the GJ plaque perimeter in CCM3KD cells, but does not physically interact, as determined by FRET analysis. It is unclear what mechanism in CCM3KD cells signals the preferential localization and accumulation of ZO-1 at Cx43 GJs over TJ localization. Changes in the accessibility of regulatory sites on Cx43 in its active state in CCM3KD cells may prevent ZO-1 trafficking within the membrane and the subsequent Claudin-5 recruitment (31). When GJ plaques are disbanded by GAP27 treatment, the preferential

conditions switch such that ZO-1 localizes to TJs and does not accumulate at Cx43 GJs. Consequently, Claudin-5 is also relocalized at the TJ and forms trans-interactions with neighboring cell Claudin-5, which seals the barrier.

Consequences in addition to GJIC-induced hyperpermeability should be considered in the pathology of fCCM3. In particular, elevated GJIC may represent a mechanism by which injury can be propagated to otherwise healthy cells, including other cell types of the neurovascular unit, pericytes and astrocytes. Several fCCM studies have demonstrated disrupted neurovascular unit architecture in which pericytes and astrocytes lose contact with endothelial cells or are completely absent (29, 30, 32–34). It is also important to highlight that fCCM3 lesions are believed to be initiated by a second hit to the functional *ccm3* allele (12, 13); however, it is not clear when in development this second hit is acquired or how many $ccm3^{-/-}$ cells are required to initiate a lesion. Whereas endothelial cell–specific ccm3KO mice develop fCCM3, and astrocyte- and neuron-specific ccm3KO mice show low or no fCCM disease penetrance, respectively, it is not yet understood whether multiple cell types are involved in the initiation and maturation of lesions (6, 35). Elevated GJIC in $ccm3^{-/-}$ cells may represent a mechanism by which $ccm3^{+/-}$ cells become damaged, despite being genetically healthy.

Of note, Cx43 is the only Cx family member that is expressed in brain endothelial cells that is affected at the protein level by CCM3KD. Several subtle, but functionally significant, differences exist between Cx family members, particularly with the existence of phosphorylation sites at the C-terminal tail that direct the Cx cycle, interactome, and downstream signaling events in response to stimuli (36). Given the accumulation of Cx43 protein without up-regulation of Cx43 transcript, it is possible that sites at the C-terminal tail that direct Cx43 degradation or endocytosis are affected by CCM3KD and result in accumulation at the membrane. ZO-1 accumulation at Cx43 GJ plaques occurs directly before the invagination of GJ plaques from the plasma membrane, representing a possible link between our observations of reduced ZO-1 interaction with Cx43 and Cx43 GJ plaque accumulation (29). Future work should focus on delineating the mechanism by which CCM3 regulates Cx43 specifically and, in addition, whether Cx43 is unique among the Cxs in its ability to regulate the establishment of TJs.

We have demonstrated that Cx43 is most robustly affected by CCM3KD and less so by CCM1 or CCM2KD. Proteomic analysis of the CCM3 interactome has revealed that 80% of total CCM3 protein is bound to the STRIPAK complex and 20% is bound to a CCM1-CCM2-CCM3 complex; thus, the STRIPAK complex is likely responsible for downstream events that are unique to CCM3 (2, 37). Given that the most robust effect of CCMKD on Cx43 protein occurs *via* the loss of CCM3, it is possible that the CCM1 and CCM2 effects on Cx43 are propagated through CCM3 *via* the CCM1-CCM2-CCM3 complex. The STRIPAK complex has many functions in the cell, regulating several phosphatases and kinases, and CCM3 is capable of regulating the activation of GCKIII kinases within the STRIPAK complex (3, 4). Elucidation of a CCM3-STRIPAK-Cx43 regulatory axis is needed. Several resident STRIPAK proteins are likely candidates, including calmodulin and PP2A. The former acts as a calcium sensor and regulates Cx43 channel opening, whereas the latter directly dephosphorylates residues Ser279/Ser282 of Cx43, which inhibits Cx43 GJ plaque formation (38–40). Elevated ERK1/2 activation is a consequence of CCM3 loss from the STRIPAK complex and causes the dysregulation of TJ structure *via* modulation cortactin protein expression, a cytoskeletal and ZO-1–interacting protein (4). Cortactin and Cx43 can be coimmunoprecipitated, but whether this occurs *via* a ZO-1 linker or a direct interaction between cortactin and ZO-1 is not clear, and how cortactin expression or organization may affect Cx43 is not known (41). In addition to the potential modulation of Cx43 *via* a STRIPAK-ERK1/2-cortactin signaling axis, Ser279/282 of Cx43 are also direct targets of ERK1/2; however, phosphorylation at these sites is typically inhibitory and, thus, may not represent the primary mechanism by which CCM3 regulates Cx43 *via* the STRIPAK complex (42, 43).

The current study has also demonstrated that lesions of $ccm3^{+/-}p53^{-/-}$ mice exhibit a progression from permeable vessels to hemorrhagic vessels, a finding that is consistent with previous murine fCCM studies (44). Gd-DTPA leakage occurs before hemorrhage, and permeable vessels have a 100% probability of hemorrhaging in the future. Histologic analysis confirmed that lesions are present in $ccm3^{+/-}p53^{-/-}$ mice in multiple stages of maturation: permeable, nonhemorrhagic stage 0 and hemorrhagic stage 1 and 2 lesions. Identifying a mechanism by which the permeability and maturation of stage 0 lesions can be blocked represents an opportunity to prevent additional pathologies.

CONCLUSIONS

Our study demonstrates that Cx43 protein is aberrantly up-regulated in developing CCM3 lesions before hemorrhage. *In vitro* data suggest that Cx43 GJs are instigators of BBB breakdown by regulating ZO-1 localization and, subsequently, limiting TJ formation and TJ transinteractions. The Cx43 GJ inhibitor, GAP27, blocked these changes. How the loss of CCM3 regulates Cx43 GJ plaque formation and signaling events that regulate Cx43–ZO-1 plaque formation should be the focus of future studies. In addition, whether *in vivo* treatment of fCCM3 mice with GAP27 can ameliorate Gd-DTPA leakage and subsequent hemorrhage is of paramount importance to determine if GAP27 or similar peptides may be candidate pharmaceutical options for patients with fCCM3. Of importance, this is the first study to our knowledge to definitively show that GJs can regulate BBB permeability in a TJ-dependent manner. Whether other mechanisms exist by which GJs can regulate permeability (*i.e.*, *via* GJIC itself) should be further investigated. FJ

ACKNOWLEDGMENTS

This work was supported by Public Health Service Grant R21NS-098066 from the National Institute of Neurological Disorders (to A.V.A.). The authors thank the Department of Radiology at The University of Michigan for the use of The Center for Molecular Imaging and the Tumor Imaging Core, which are supported, in part, by Comprehensive Cancer Center U.S. National Institutes of Health (NIH) Grant P30-CA046592. The authors also thank the Single Molecule Analysis in Real-Time Center of the University of Michigan, seeded by National Science Foundation MRI-R2-ID award DBI-0959823 to Nils G. Walter, as well as J. Damon Hoff for training, technical advice, and the use of the Olympus STORM-capable microscope. Histology slide scanning was performed at the Department of Pathology Core Flow Cytometry Laboratory and Slide Scanning Services. The authors declare no conflicts of interest.

AUTHOR CONTRIBUTIONS

A. M. Johnson performed experiments, contributed to study design and writing of the manuscript; J. P. Roach, A. Hu, S. M. Stamatovic performed experiments and contributed to data analysis and discussion; M. R. Zochowski contributed to microinjection measurements and data discussion; R. F. Keep contributed to data discussion and reviewed and edited the article; and A. V. Andjelkovic designed the study, reviewed data, contributed to writing the manuscript, and acts as guarantor for the manuscript.

REFERENCES

1. Mikati, A. G., Khanna, O., Zhang, L., Girard, R., Shenkar, R., Guo, X., Shah, A., Larsson, H. B., Tan, H., Li, L., Wishnoff, M. S., Shi, C., Christoforidis, G. A., and Awad, I. A. (2015) Vascular permeability in cerebral cavernous malformations. *J. Cereb. Blood Flow Metab.* **35**, 1632–1639
2. Goudreault, M., D'Ambrosio, L. M., Kean, M. J., Mullin, M. J., Larsen, B. G., Sanchez, A., Chaudhry, S., Chen, G. I., Sicheri, F., Nesvizhskii, A. I., Aebersold, R., Raught, B., and Gingras, A. C. (2009) A PP2A phosphatase high density interaction network identifies a novel striatin-interacting phosphatase and kinase complex linked to the cerebral cavernous malformation 3 (CCM3) protein. *Mol. Cell. Proteomics* **8**, 157–171
3. Hwang, J., and Pallas, D. C. (2014) STRIPAK complexes: structure, biological function, and involvement in human diseases. *Int. J. Biochem. Cell Biol.* **47**, 118–148
4. Stamatovic, S. M., Sladojevic, N., Keep, R. F., and Andjelkovic, A. V. (2015) PDCD10 (CCM3) regulates brain endothelial barrier integrity in cerebral cavernous malformation type 3: role of CCM3-ERK1/2-cortactin cross-talk. *Acta Neuropathol.* **130**, 731–750
5. McDonald, D. A., Shenkar, R., Shi, C., Stockton, R. A., Akers, A. L., Kucherlapati, M. H., Kucherlapati, R., Brainer, J., Ginsberg, M. H., Awad, I. A., and Marchuk, D. A. (2011) A novel mouse model of cerebral cavernous malformations based on the two-hit mutation hypothesis recapitulates the human disease. *Hum. Mol. Genet.* **20**, 211–222
6. He, Y., Zhang, H., Yu, L., Gunel, M., Boggon, T. J., Chen, H., and Min, W. (2010) Stabilization of VEGFR2 signaling by cerebral cavernous malformation 3 is critical for vascular development. *Sci. Signal.* **3**, ra26
7. Martinez, A. D., Hayrapetyan, V., Moreno, A. P., and Beyer, E. C. (2002) Connexin43 and connexin45 form heteromeric gap junction channels in which individual components determine permeability and regulation. *Circ. Res.* **90**, 1100–1107
8. Gabriels, J. E., and Paul, D. L. (1998) Connexin43 is highly localized to sites of disturbed flow in rat aortic endothelium but connexin37 and connexin40 are more uniformly distributed. *Circ. Res.* **83**, 636–643
9. Bruzzone, R., Haefliger, J. A., Gimlich, R. L., and Paul, D. L. (1993) Connexin40, a component of gap junctions in vascular endothelium, is restricted in its ability to interact with other connexins. *Mol. Biol. Cell* **4**, 7–20
10. Zhang, J., Yang, G.-M., Zhu, Y., Peng, X.-Y., Li, T., and Liu, L.-M. (2015) Role of connexin 43 in vascular hyperpermeability and relationship to Rock1-MLC20 pathway in septic rats. *Am. J. Physiol. Lung Cell. Mol. Physiol.* **309**, L1323–L1332
11. Kandasamy, K., Escue, R., Manna, J., Adebiyi, A., and Parthasarathi, K. (2015) Changes in endothelial connexin 43 expression inversely correlate with microvessel permeability and VE-cadherin expression in endotoxin-challenged lungs. *Am. J. Physiol. Lung Cell. Mol. Physiol.* **309**, L584–L592
12. Akers, A. L., Johnson, E., Steinberg, G. K., Zabramski, J. M., and Marchuk, D. A. (2009) Biallelic somatic and germline mutations in cerebral cavernous malformations (CCMs): evidence for a two-hit mechanism of CCM pathogenesis. *Hum. Mol. Genet.* **18**, 919–930
13. Pagenstecher, A., Stahl, S., Sure, U., and Felbor, U. (2009) A two-hit mechanism causes cerebral cavernous malformations: complete inactivation of CCM1, CCM2 or CCM3 in affected endothelial cells. *Hum. Mol. Genet.* **18**, 911–918
14. Kazakoff, P. W., McGuire, T. R., Hoie, E. B., Cano, M., and Iversen, P. L. (1995) An *in vitro* model for endothelial permeability: assessment of monolayer integrity. *In Vitro Cell. Dev. Biol. Anim.* **31**, 846–852
15. Dimitrijevic, O. B., Stamatovic, S. M., Keep, R. F., and Andjelkovic, A. V. (2006) Effects of the chemokine CCL2 on blood-brain barrier permeability during ischemia-reperfusion injury. *J. Cereb. Blood Flow Metab.* **26**, 797–810
16. Aasen, T. (2015) Connexins: junctional and non-junctional modulators of proliferation. *Cell Tissue Res.* **360**, 685–699
17. Olk, S., Zoidl, G., and Dermietzel, R. (2009) Connexins, cell motility, and the cytoskeleton. *Cell Motil. Cytoskeleton* **66**, 1000–1016
18. Chaytor, A. T., Evans, W. H., and Griffith, T. M. (1998) Central role of heterocellular gap junctional communication in endothelium-dependent relaxations of rabbit arteries. *J. Physiol.* **508**, 561–573
19. Wang, N., De Vuyst, E., Ponsaerts, R., Boengler, K., Palacios-Prado, N., Wauman, J., Lai, C. P., De Bock, M., Decrock, E., Bol, M., Vinken, M., Rogiers, V., Tavernier, J., Evans, W. H., Naus, C. C., Bukauskas, F. F., Sipido, K. R., Heusch, G., Schulz, R., Bultynck, G., and Leybaert, L. (2013) Selective inhibition of Cx43 hemichannels by Gap19 and its impact on myocardial ischemia/reperfusion injury. *Basic Res. Cardiol.* **108**, 309–325
20. Giepmans, B. N., and Moolenaar, W. H. (1998) The gap junction protein connexin43 interacts with the second PDZ domain of the zona occludens-1 protein. *Curr. Biol.* **8**, 931–934
21. Jin, C., Martyn, K. D., Kurata, W. E., Warn-Cramer, B. J., and Lau, A. F. (2004) Connexin43 PDZ2 binding domain mutants create functional gap junctions and exhibit altered phosphorylation. *Cell Commun. Adhes.* **11**, 67–87
22. Segretain, D., Fiorini, C., Decrouy, X., Defamie, N., Prat, J. R., and Pointis, G. (2004) A proposed role for ZO-1 in targeting connexin 43 gap junctions to the endocytic pathway. *Biochimie* **86**, 241–244
23. Fanning, A. S., and Anderson, J. M. (2009) Zonula occludens-1 and -2 are cytosolic scaffolds that regulate the assembly of cellular junctions. *Ann. N. Y. Acad. Sci.* **1165**, 113–120
24. Nitta, T., Hata, M., Gotoh, S., Seo, Y., Sasaki, H., Hashimoto, N., Furuse, M., and Tsukita, S. (2003) Size-selective loosening of the blood-brain barrier in claudin-5-deficient mice. *J. Cell Biol.* **161**, 653–660
25. Krause, G., Winkler, L., Mueller, S. L., Haseloff, R. F., Piontek, J., and Blasig, I. E. (2008) Structure and function of claudins. *Biochim. Biophys. Acta* **1778**, 631–645
26. O'Donnell III, J. J., Birukova, A. A., Beyer, E. C., and Birukov, K. G. (2014) Gap junction protein connexin43 exacerbates lung vascular permeability. *PLoS One* **9**, e100931
27. Lin, J. H., Weigel, H., Cotrina, M. L., Liu, S., Bueno, E., Hansen, A. J., Hansen, T. W., Goldman, S., and Nedergaard, M. (1998) Gap-junction-mediated propagation and amplification of cell injury. *Nat. Neurosci.* **1**, 494–500
28. De Bock, M., Culot, M., Wang, N., Bol, M., Decrock, E., De Vuyst, E., da Costa, A., Dauwe, I., Vinken, M., Simon, A. M., Rogiers, V., De Ley, G., Evans, W. H., Bultynck, G., Dupont, G., Cecchelli, R., and Leybaert, L. (2011) Connexin channels provide a target to manipulate brain endothelial calcium dynamics and blood-brain barrier permeability. *J. Cereb. Blood Flow Metab.* **31**, 1942–1957
29. Hunter, A. W., Barker, R. J., Zhu, C., and Gourdie, R. G. (2005) Zonula occludens-1 alters connexin43 gap junction size and organization by influencing channel accretion. *Mol. Biol. Cell* **16**, 5686–5698

30. Rhett, J. M., Jourdan, J., and Gourdie, R. G. (2011) Connexin 43 connexon to gap junction transition is regulated by zonula occludens-1. *Mol. Biol. Cell* **22**, 1516–1528
31. Solan, J. L., and Lampe, P. D. (2009) Connexin43 phosphorylation: structural changes and biological effects. *Biochem. J.* **419**, 261–272
32. Clatterbuck, R. E., Eberhart, C. G., Crain, B. J., and Rigamonti, D. (2001) Ultrastructural and immunocytochemical evidence that an incompetent blood-brain barrier is related to the pathophysiology of cavernous malformations. *J. Neurol. Neurosurg. Psychiatry* **71**, 188–192
33. Tu, J., Stoodley, M. A., Morgan, M. K., and Storer, K. P. (2005) Ultrastructural characteristics of hemorrhagic, nonhemorrhagic, and recurrent cavernous malformations. *J. Neurosurg.* **103**, 903–909
34. Tanriover, G., Sozen, B., Seker, A., Kilic, T., Gunel, M., and Demir, N. (2013) Ultrastructural analysis of vascular features in cerebral cavernous malformations. *Clin. Neurol. Neurosurg.* **115**, 438–444
35. Louvi, A., Chen, L., Two, A. M., Zhang, H., Min, W., and Günel, M. (2011) Loss of cerebral cavernous malformation 3 (Ccm3) in neuroglia leads to CCM and vascular pathology. *Proc. Natl. Acad. Sci. USA* **108**, 3737–3742
36. Leithe, E., Mesnilb, M., and Aasen, T. (2018) The connexin 43 C-terminus: a tail of many tales. *Biochim. Biophys. Acta* **1860**, 48–64
37. Hilder, T. L., Malone, M. H., Bencharit, S., Colicelli, J., Haystead, T. A., Johnson, G. L., and Wu, C. C. (2007) Proteomic identification of the cerebral cavernous malformation signaling complex. *J. Proteome Res.* **6**, 4343–4355
38. Zhou, Y., Yang, W., Lurtz, M. M., Ye, Y., Huang, Y., Lee, H. W., Chen, Y., Louis, C. F., and Yang, J. J. (2007) Identification of the calmodulin binding domain of connexin 43. *J. Biol. Chem.* **282**, 35005–35017
39. Zou, J., Salarian, M., Chen, Y., Veenstra, R., Louis, C. F., and Yang, J. J. (2014) Gap junction regulation by calmodulin. *FEBS Lett.* **588**, 1430–1438
40. Wu, J., Taylor, R. N., and Sidell, N. (2013) Retinoic acid regulates gap junction intercellular communication in human endometrial stromal cells through modulation of the phosphorylation status of connexin 43. *J. Cell. Physiol.* **228**, 903–910
41. Vitale, M. L., Akpovi, C. D., and Pelletier, R. M. (2009) Cortactin/tyrosine-phosphorylated cortactin interaction with connexin 43 in mouse seminiferous tubules. *Microsc. Res. Tech.* **72**, 856–867
42. Riquelme, M. A., Burra, S., Kar, R., Lampe, P. D., and Jiang, J. X. (2015) Mitogen-activated protein kinase (MAPK) activated by prostaglandin E_2 phosphorylates connexin 43 and closes osteocytic hemichannels in response to continuous flow shear stress. *J. Biol. Chem.* **290**, 28321–28328
43. Ruch, R. J., Trosko, J. E., and Madhukar, B. V. (2001) Inhibition of connexin43 gap junctional intercellular communication by TPA requires ERK activation. *J. Cell. Biochem.* **83**, 163–169
44. Stockton, R. A., Shenkar, R., Awad, I. A., and Ginsberg, M. H. (2010) Cerebral cavernous malformations proteins inhibit Rho kinase to stabilize vascular integrity. *J. Exp. Med.* **207**, 881–896

Received for publication July 21, 2017.
Accepted for publication December 18, 2017.